International Journal of Multiphase Flow 200 (2026) 105736

Contents lists available at ScienceDirect

International Journal of Multiphase Flow

journal homepage: www.elsevier.com/locate/ijmulflow

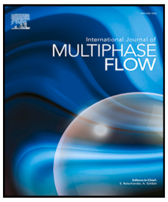

Research Paper

Classification of primary breakup modes for dual gas-assisted annular sheet nozzles

Juliana Richter [a,*], Tobias Jakobs [a], Frederik Scheiff [a,b], Thomas Kolb [a,b]

[a] Institute for Technical Chemistry, Hermann-von-Helmholtz-Platz 1, Eggenstein-Leopoldshafen, 76344, Germany
[b] Engler-Bunte-Institut, Fuel Technology, Engler-Bunte-Ring 7, Karlsruhe, 76131, Germany

ARTICLE INFO

Keywords:
Sheet atomization
Primary breakup
Breakup regime
Liquid sheet thickness
Liquid mass flow rate

ABSTRACT

This study aims for the systematic characterization of the primary breakup pattern of gas-assisted annular sheet nozzles featuring two co-flowing gas streams (dual gas-assisted annular sheet nozzles). Three nozzles with different liquid sheet thickness (1–3 mm) but constant gas orifice areas were applied. Water was used as liquid phase. The liquid as well as both gas streams were varied independently. Primary breakup was captured utilizing high-speed imaging.

Besides known breakup modes already described in literature, new modes were observed and described as function of inner/outer gas momentum flow rate and liquid velocity for each sheet thickness. Breakup modes were categorized into bubble-induced modes – characterized by the formation of a bubble – and non-bubble-induced modes, where bubble formation is suppressed. A comprehensive mapping and detailed description of the primary breakup of dual gas-assisted annular sheet nozzles is presented, offering new insights into the interplay between gas and liquid flow rates and nozzle geometry.

Furthermore, an empirical approach was developed to calculate the inner and outer gas momentum flow rates required to achieve technically relevant breakup regimes across varying liquid mass flow rates. These findings establish a basis for liquid mass flow scaling and support the design and optimization of atomization systems for technical applications.

1. Introduction

Gas-assisted nozzles are utilized in a variety of industrial processes, e.g., combustion (Haidn and Habiballah, 2003; Alajmi et al., 2019), gasification (Carisson et al., 2009; Risberg and Marklund, 2009), spray cooling (Muthukrishnan et al., 2023; Zhao et al., 2025), gas cleaning (Rajmohan et al., 2008; Cejpek et al., 2025), food processing (Mlkvik et al., 2015; Martínez et al., 2025) and agricultural applications (Yuan et al., 2023; Ye et al., 2025). In all these processes, the nozzle geometry, along with the fluid properties and operating conditions, significantly influences the primary breakup pattern. This, in turn, determines the resulting droplet size and spray distribution (Wachter et al., 2021a,b; Kuznetsov et al., 2024) and governs subsequent heat and mass transfer steps.

For instance, in the context of agricultural fertilizer spraying, Wang et al. (2023) and Zhou et al. (2024) demonstrated that nozzle geometry substantially affects droplet size distribution, spray coverage and drift reduction. In entrained flow gasifiers, Haas et al. (2023, 2025) showed that spray parameters – such as spray angle, droplet velocity and droplet size – significantly influence fuel evaporation within the flame boundaries. These spray parameters are governed not only by secondary breakup, but also by primary breakup, which essentially affects the overall spray characteristics.

Importantly, the nature and dynamics of secondary breakup are strongly influenced by the characteristics of the primary breakup, making a detailed understanding of the initial disintegration process essential for predicting and controlling overall spray characteristics. This understanding is also fundamental for numerical modeling approaches, including the development of a Karlsruhe Institute of Technology, which aims to predict spray characteristics based on a detailed simulation of primary breakup process. In this context, Zhang et al. (2023) conducted a detailed numerical simulation of the primary breakup as a first step.

A widely studied configuration is the twin-fluid jet nozzle, in which a central liquid jet is surrounded by an annular gas stream (Chigier

---

* Corresponding author.

E-mail addresses: Juliana.Richter@kit.edu (J. Richter), Tobias.Jakobs@kit.edu (T. Jakobs), Frederik.Scheiff@kit.edu (F. Scheiff), Thomas.Kolb@kit.edu (T. Kolb).

URL: https://www.itc.kit.edu/390.php (J. Richter).

https://doi.org/10.1016/j.ijmultiphaseflow.2026.105736
Received 13 December 2025; Received in revised form 27 March 2026; Accepted 10 April 2026

and Faragó, 1992; Lasheras and Hopfinger, 2000; Sänger et al., 2014; Zhao et al., 2014a,b). However, scaling the liquid mass flow rate of these nozzles is limited to either increasing the liquid velocity through a single nozzle or enlarging the liquid jet diameter d_l while keeping the liquid velocity constant — both approaches entail significant drawbacks (Lefebvre, 1992; Leroux et al., 2007). Higher liquid velocities reduce the relative velocity between gas and liquid phase and diminish aerodynamic shear forces, thereby compromising atomization efficiency and increasing abrasion risk when handling particle-laden liquids. Increasing d_l results in thicker liquid jets with lower surface-to-volume ratios, which reduce the available interface for gas–liquid interaction. Consequently, the gas stream transfers most of its momentum to the outer liquid layers before reaching the jet core, further impairing atomization performance (Varga et al., 2003; Wachter et al., 2022).

To overcome the limitations of conventional twin-fluid jet nozzles, the twin-fluid annular sheet nozzle was investigated, where the liquid is discharged as an annular sheet and atomized by a central gas jet. A key advantage is that the inner gas exit diameter $d_\mathrm{g,i}$ can be increased while maintaining a constant liquid sheet thickness s_l - thereby enlarging the liquid exit orifice area and enabling higher liquid mass flow rates without altering the liquid velocity. To further enhance atomization performance, an additional shear layer can be introduced via an outer annular gas stream, resulting in a dual gas-assisted annular sheet nozzle. Studies show that this design achieves superior atomization performance and minimal droplet sizes for a given energy input (Wachter et al., 2021a; Ibrahim and Jog, 2008; Wahono et al., 2008).

The present work therefore focuses on the primary breakup of dual gas-assisted annular sheet nozzles to elucidate the fundamental mechanisms governing droplet formation and atomization.

A brief review of established primary breakup regimes for dual gas-assisted annular sheet nozzles is necessary to set the scope of the present work.

Only a limited group of researchers has systematically investigated the primary breakup of sheet atomization driven by two gas streams. These studies are limited to thin liquid sheets below 1 mm. The most frequently observed modes include **Rayleigh** and **bubble breakup**, as well as the **Christmas tree** and the **prompt atomization regime** (Wahono et al., 2008; Lavergne et al., 1993; Carvalho and Heitor, 1998; Adzic et al., 2001; Fu et al., 2003; Leboucher et al., 2010) (Fig. 2). These regimes are repeatedly observed across the literature, although not all are addressed in every publication. Nevertheless, these four modes represent the most frequently cited and broadly accepted breakup regimes in the context of dual gas-assisted annular sheet nozzles.

The **Rayleigh breakup mode**, originally described by Kendall (1986) for twin-fluid annular sheet nozzles under the term train of shells, has also been observed in twin-fluid jet nozzles by Chigier and Faragó (1992), who introduced the term **Rayleigh breakup**. Although the terminology is shared, the visual appearance of this mode differs significantly between jet and annular sheet nozzles, despite both being governed by Kelvin–Helmholtz instabilities. This mode has since been confirmed for twin-fluid annular sheet nozzles by numerous authors (Choi and Lee, 1997; Sevilla et al., 2005; Gañán-Calvo et al., 2006; Sikka et al., 2021).

The **bubble breakup mode**, initially reported by Choi and Lee (1997) for twin-fluid annular sheet nozzles, was subsequently corroborated by Zhao et al. (2015) for a similar nozzle configuration.

The **Christmas tree regime**, introduced by Adzic et al. (2001), is unique in that it requires both inner and outer gas stream. It is suggested that this regime is governed by an inner gas-induced bubble that is compressed by the outer gas stream until the bubble wall ruptures. Although originally described for dual gas sheet configurations, this regime is referred to by Zhao et al. (2015) in the context of a twin-fluid annular sheet nozzle with only a single gas stream — raising questions about the underlying mechanisms and the potential for similar breakup patterns under different aerodynamic conditions.

Despite the distinct flow configurations, the **prompt atomization regime** – originally described by Lefebvre (1992) for twin-fluid jet nozzles – shows a similar visual manifestation for dual gas-assisted annular sheet nozzles, indicating comparable breakup mechanisms. Among all reported breakup modes, it is the only one for which the visual characteristics remain consistent regardless of jet or annular sheet nozzle configuration.

In addition to the commonly accepted breakup regimes, the authors who investigated the primary breakup of annular sheet nozzles driven by two gas streams also proposed a range of additional breakup modes (Lavergne et al., 1993; Carvalho and Heitor, 1998; Adzic et al., 2001; Chatterjee et al., 2015). Many of these appear exclusively in their respective publications and have not been widely adopted or experimentally validated. These newly introduced regimes often exhibit visual similarities to established ones. For instance, the *early breakup* described by Chatterjee et al. (2015) and the *atomization regime* introduced by Adzic et al. (2001) closely resemble the **prompt atomization regime**. When considering industry-relevant breakup modes – typically characterized by the formation of fine sprays suitable for technical applications – it becomes evident that many of the uniquely named regimes, such as *necklace* and *onion breakup* described by Chatterjee et al. (2015), as well as the widely known **Rayleigh** and **bubble breakup**, lack practical relevance. These regimes are associated with low aerodynamic energy input, occurring when one or both gas streams are insufficient to induce effective liquid disintegration.

A systematic framework for breakup regime classification was proposed by Leboucher et al. (2010) and Chatterjee et al. (2015). Regime classifications aim to correlate breakup modes with operating conditions, fluid properties and nozzle geometry. In general, by providing a structured framework, regime maps can serve as a valuable tool for identifying technically relevant operating ranges and nozzle designs to achieve specific spray characteristics.

Comparing their results with Fu et al. (2003) and Wahono et al. (2008), Leboucher et al. (2010) presented a classification plotting total gas versus liquid momentum flow rate:

$$\dot{J}_\mathrm{g,tot} = \dot{J}_\mathrm{g,i} + \dot{J}_\mathrm{g,o} \tag{1}$$

$$\dot{J}_\mathrm{j} = v_\mathrm{j}^2 \cdot \rho_\mathrm{j} \cdot A_\mathrm{j} \tag{2}$$

with momentum flow rate ($\dot{J}$), velocity (v), density (ρ) and exit orifice area (A). Subscript g indicates the gas and liquid phase, while i and o refer to the inner and outer gas stream, respectively. The subscript j may represent either the inner gas (g,i), the outer gas stream (g,o) or the liquid phase (l). The regime map by Leboucher et al. (2010) does not distinguish between the inner and outer gas flow, even though several studies suggest that the inner gas stream may play a dominant role in the breakup dynamics, e.g. Ibrahim and Jog (2008) and Carvalho and Heitor (1998).

Chatterjee et al. (2015) developed a three-dimensional regime map, using the inner and outer gas Reynolds number ($Re_\mathrm{g,i}$, $Re_\mathrm{g,o}$), as well as the liquid Weber number (We_l) as governing parameters:

$$Re_\mathrm{j} = \frac{v_\mathrm{j} \cdot \rho_\mathrm{j} \cdot L_\mathrm{c,j}}{\eta_\mathrm{j}} \tag{3}$$

$$We_\mathrm{l} = \frac{v_\mathrm{l}^2 \cdot \rho_\mathrm{l} \cdot L_\mathrm{c,l}}{\sigma} \tag{4}$$

with characteristic length (L_c), dynamic viscosity (η) and surface tension (σ). In this study, L_c is defined as the exit diameter (d), which corresponds to the respective channel (inner gas, liquid or outer gas) of the nozzle. Although the influence of both gas streams was explicitly considered in this regime classification, Chatterjee et al. (2015) identified five distinct breakup modes, none of them — except for the *early breakup mode* (analogous to the **prompt atomization mode**) align with

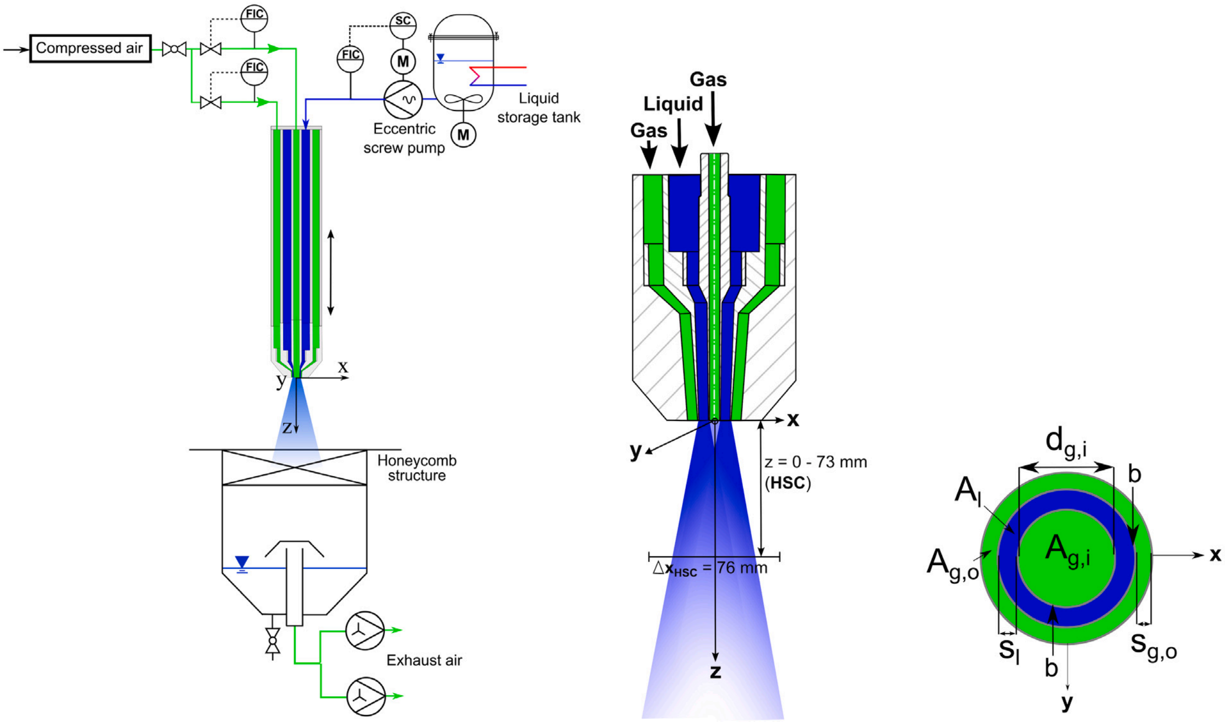

(i) (ii) (iii)

Fig. 1. Schematic of the experimental setup, atmospheric spray test rig (ATMO) (i); nozzle cross-sectional view (ii); nozzle top view (iii).

the established breakup regimes. This highlights the incompleteness in regime classification across the literature and complicates direct comparisons between regime maps.

To address the lack of a consistent framework for dual gas-assisted sheet atomization, this study systematically investigates the influence of key parameters – namely, the independently varied inner and outer gas stream, the liquid mass flow rate and the liquid sheet thickness – on primary breakup. The primary objective is to establish regime maps as a function of inner and outer gas momentum flow rate, liquid velocity and liquid sheet thickness, thereby identifying the parameter space relevant to technical applications and elucidating the mechanisms driving regime transitions.

2. Methodology

2.1. Experimental setup

Spray formation was investigated using three custom-designed dual gas-assisted annular sheet nozzles with varying liquid sheet thicknesses, hereafter referred to as sheet nozzles. Each axisymmetric nozzle consisted of three concentric, coaxial flow passages (see Fig. 1(ii)/(iii)). Compressed air was supplied through the innermost and outermost channels, while the liquid was injected via the intermediate annular gap. The nozzle geometry employed parallel flow channels, facilitating comparison with previous studies (e.g., Leboucher et al., 2010; Zhao et al., 2015). The separating walls between adjacent flow passages were reduced to $b = 0.1$ mm to minimize flow disturbances, as recommended by Tian et al. (2014).

To allow for an isolated variation of sheet thickness without altering gas momentum input under constant operating conditions, the inner and outer gas exit areas ($A_{g,i}$ and $A_{g,o}$) were kept constant within the limits of manufacturing accuracy (maximum deviation < 2.2 %) by adjusting the outer gas gap widths ($s_{g,o}$), as summarized in Table 1. The inner gas was injected through a central orifice with a diameter of $d_{g,i}$ = 3 mm, while the outer gas was supplied through annular slits. The liquid sheet thickness s_l was varied in the steps 1, 2 and 3 mm. Experiments were conducted at the atmospheric spray test rig (ATMO), described in detail by Sänger (2018) and shown in Fig. 1(i). The sheet nozzles were mounted on a dedicated three-fluid lance. Water at 20 °C was atomized using pressurized air. Liquid supply was provided by an eccentric screw pump (mass flow range: 5–100 kg h^{-1}), with flow rate monitored and regulated using a Coriolis-type mass flow and density meter (Bronkhorst High-Tech B.V.). Compressed air was delivered through two independently controlled lines, each equipped with hot-wire anemometers and precision control valves (Bronkhorst High-Tech B.V.), covering gas mass flow rates of 0.4–20 kg h^{-1} (inner) and 10–100 kg h^{-1} (outer). To minimize droplet recirculation, two high-capacity exhaust systems were installed. Additionally, a flow straightener (honeycomb structure) was placed at the collection tank inlet. The velocities of both gas and liquid phases were calculated from the prescribed mass flow rates and the known nozzle exit areas using incompressible densities at ambient conditions. As documented in Table 3, the maximum velocity observed in either phase is 76 m s^{-1} (corresponding to a Mach number of approximately 0.2), compressibility effects are negligible throughout the study (Bohl and Elmendorf, 2014).

Table 1
Nozzle data (Nozzle 1–3).

	$d_{g,i}$ in mm	s_l in mm	$s_{g,o}$ in mm
Nozzle 1	3	1	4.1
Nozzle 2	3	2	3.6
Nozzle 3	3	3	3.1

Primary atomization was captured using a high-speed camera (Phantom v1840, Vision Research) in backlight configuration, illuminated by a high-intensity LED array (LED 4438-Boost, High Speed Vision GmbH, peak power: 1000 W). The high-speed camera (HSC) settings are listed in Table 2). Frame rates reported in imaging-based investigations of primary liquid sheet breakup span a broad range,

Table 2
High-speed camera settings.

Setting	
Resolution in px	2048 × 1952
Field of view in mm^2	76 × 73
z position in mm	0
Focal length in mm	105
Frame rate in fps	4500
Aperture	8
ISO	3200
Shutter speed in μs	1.5

Table 3
Operating conditions of the experiments for the parametric study for each nozzle configuration (s_l = 1–3 mm).

$\dot{M}_\mathrm{g,i}$ in kg h^{-1}	$v_\mathrm{g,i}$ in m s^{-1}	$\dot{M}_\mathrm{l}$ in kg h^{-1}	v_l in m s^{-1}	$\dot{M}_\mathrm{g,o}$ in kg h^{-1}	$v_\mathrm{g,o}$ in m s^{-1}
0.4/0.6/0.8/ 1.0/1.2/1.4/ 1.6/1.8/2.0	13–65	30/60/90	0.1–1.9	5/6/7/8/ 9/10/15/20/ 25/30/35/40	7–76

typically within 10^2–10^4 fps (e.g., Wahono et al. (2008), Leboucher et al. (2010), Chatterjee et al. (2015) and Zhao et al. (2014c)). Higher frame rates up to 10^5 fps have also been reported in related atomization studies (e.g., Fu et al., 2003; Peteinaris and Terzis, 2025). As the present work focuses on the classification of large-scale breakup regimes, which remain stationary over 1000 recorded frames for each operating condition, the selected frame rate of 4.5 kfps is sufficient.

2.2. Investigated configurations

In order to investigate the primary breakup in a comprehensive parametric study, the inner and outer gas mass flow rates ($\dot{M}_\mathrm{g,i}$ and $\dot{M}_\mathrm{g,o}$), the liquid mass flow rate ($\dot{M}_\mathrm{l}$), as well as the liquid sheet thickness (s_l) were systematically varied, see Table 3. Depending on the flow conditions and the liquid sheet thickness, various breakup modes were observed. Based on these observations, regime classifications are presented as functions of the inner/outer gas momentum flow rate ($\dot{J}_\mathrm{g,i}$, $\dot{J}_\mathrm{g,o}$), the liquid velocity (v_l) and the liquid sheet thickness.

Since atomization is primarily controlled by the momentum transfer of the assisting gas, the gas momentum flow rate is a widely accepted parameter to characterize spray formation and breakup (Leboucher et al., 2010; Sivakumar and Kulkarni, 2011). In addition, the liquid velocity and liquid sheet thickness are considered, as the results indicate that a two-dimensional mapping based exclusively on gas momentum flow rates is not sufficient to fully resolve the observed breakup regimes.To ensure transparency of the classification method, the identification of breakup modes was based on the complete time sequences consisting of 1000 frames for each operating condition. Near regime boundaries, breakup patterns of two adjacent modes may appear within the same sequence. In such cases, the final regime label was assigned according to the breakup mode that occurred more frequently over the full set of frames.

3. Results and discussion

In the following, the distinct primary breakup modes observed (Fig. 2) are described in conjunction with the corresponding regime maps (Figs. 3–5 and A.1) to illustrate the relationships between operating parameters, liquid sheet thickness and breakup pattern.

3.1. Influence of gas momentum flow rates

As a first step, the influence of inner and outer gas momentum flow rate is analyzed based on the breakup mode classification shown in Fig. 3 as a representative example, corresponding to a liquid sheet thickness of 1 mm and a liquid velocity of 1.3 m s^{-1}.

In general, axisymmetric oscillations develop on the liquid surface immediately after discharge from the nozzle. These oscillations arise from Kelvin–Helmholtz instabilities and lead to the pinching off of the liquid sheet, resulting in an encapsulation of the core gas and thereby initiating the formation of bubbles, see Fig. 2(i)–(iii). While an increase in inner gas momentum flow rate promotes a stronger bubble inflation, the outer gas stream exerts a compressive effect by impinging from above. As long as the bubble remains connected to the liquid column, its expansion occurs predominantly in the radial direction, with limited axial growth. This primarily radial expansion can be attributed to the stabilizing influence of surface tension in the axial direction, as well as the geometric constraint imposed by the liquid column, which restricts axial elongation. This expansion continues until rupture occurs, resulting in the lateral ejection of ligaments and droplets.

As long as the formed bubbles remain intact, the breakup pattern corresponds to the classical **Rayleigh mode** (Fig. 2(i)), which resembles a bubble train and is typically observed under low inner (<0.005 N) and outer (<0.04 N) gas momentum flow rates (see Fig. 3). Increasing inner gas momentum flow rate promotes the coalescence of individual bubbles into larger ones, preceding the onset of rupture.

Bubble rupture leads to the **bubble breakup mode**. Within this regime, two distinct sub-modes can be distinguished: the **inner gas-driven bubble breakup mode** (Fig. 2(ii)), characterized by the complete bursting of the bubble due to the high momentum of the inner gas flow, and the **outer gas-driven bubble breakup mode** (Fig. 2(iii)), where the bubble bursts due to high outer aerodynamic forces. In both modes, bubble disintegration initially produces small droplets and an annular rim, which undergoes secondary breakup into larger droplets at larger axial distance from the nozzle, while the connecting liquid column forms satellite droplets.

As the inner gas momentum flow rate further increases, the breakup transitions into the **pure pulsating mode** (Fig. 2(iv)), originally described by Choi and Lee (1997). This mode is defined by ring-shaped liquid layers, which further disintegrate, resulting in larger droplets at the spray boundary. It emerges from the **inner gas-driven bubble breakup mode**, when the inner gas momentum flow rate becomes sufficiently dominant to cause high-frequency bubble bursting. Due to the low outer gas momentum flow rate, only an annular liquid rim remains, which fragments into ligaments and droplets. This mode is therefore characterized by a high frequency of bubble formation and bursting. Starting from the **outer gas-driven bubble breakup mode**, an increase in outer gas momentum flow rate leads to the **Christmas tree mode** (Fig. 2(v)). It also originates from bursting bubbles, but is distinguished by large, vertically aligned trunk-like fragments concentrated along the spray centerline. These are caused by relatively weak inner aerodynamic forces, which limit disintegration close to the centerline.

With further increase of the outer gas momentum flow rate, the breakup transitions into the **pulsating atomization mode** (Fig. 2(vi)). In this regime, bubbles are periodically torn apart directly below the nozzle exit, producing alternating spray regions: wide, radially spread sections dominated by ligament fragmentation, and narrower ones where breakup occurs without bubble formation. This leads to a time-dependent, pulsating spray pattern. This mode was observed at high outer gas momentum flow rates (>0.2 N) for all investigated inner gas momentum flow rates, indicating its robustness across a wide range of operating conditions (Fig. 3).

As shown in Fig. 3, increasing both inner and outer gas momentum flow rate – before the transition to the **pulsating atomization mode** – leads to the occurrence of the **membrane-dominated breakup mode** (Fig. 2(vii)). In this regime, a detached bubble inflates into a large, thin membrane structure that primarily expands radially. When the outer gas momentum flow rate is dominant, the membrane adopts an inverted mushroom-like shape, resulting from strong aerodynamic compression

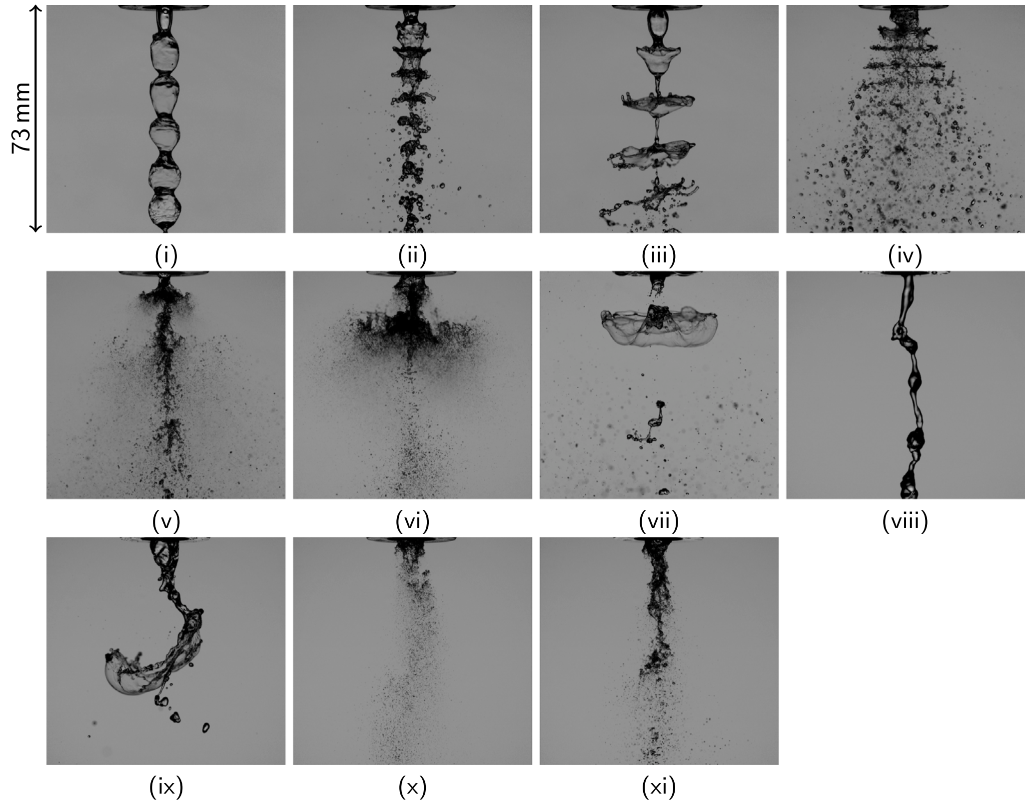

Fig. 2. Primary breakup modes (i–xi) shown in the order of their appearance in the text, Rayleigh mode (i); inner gas-driven bubble breakup mode (ii); outer gas-driven bubble breakup mode (iii); pure pulsating mode (iv); Christmas tree mode (v); pulsating atomization mode (vi); membrane-dominated breakup mode (vii); beads-on-a-string mode (viii); membrane-like breakup mode (ix); prompt atomization mode (x) and fiber type breakup (xi).

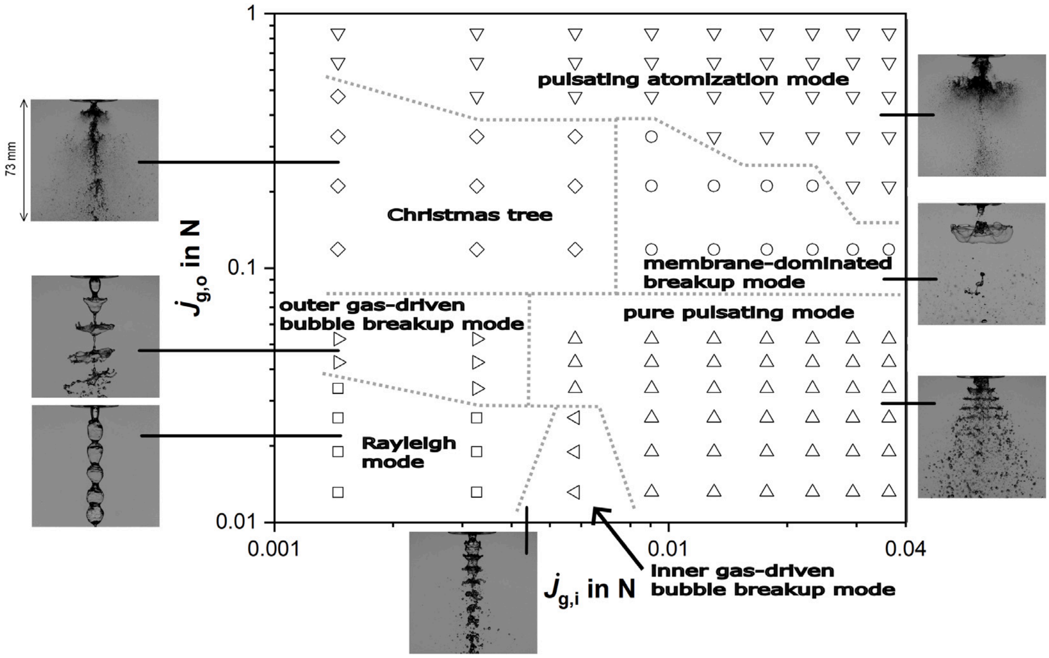

Fig. 3. Breakup mode classification from HSC images for $s_l = 1$ mm, shown as function of inner and outer gas momentum flow rate ($\dot{J}_{g,i}$ and $\dot{J}_{g,o}$) for a liquid velocity $v_l = 1.3$ m s^{-1} (liquid mass flow rate $\dot{M}_l = 60$ kg h^{-1}).

from the outside. As the inner gas momentum flow rate increases, the structure inflates more uniformly and the mushroom shape becomes less pronounced. In contrast, in the **pulsating atomization mode**, the aerodynamic forces are sufficiently strong to prevent the formation of large membranes altogether, instead leading to rapid, periodic ligament ejection.

Previous studies suggested that the inner gas stream exerts the dominant influence on breakup pattern (Carvalho and Heitor, 1998; Shen and Li, 1996). Fig. 3 clearly demonstrates that increasing the momentum flow rate of either gas stream triggers distinct transitions between breakup modes. For instance, the **pure pulsating mode** emerges exclusively when the inner gas momentum flow rate is increased, whereas the **Christmas tree mode** appears only when the outer gas momentum flow rate is increased. Neither mode can be obtained by increasing the momentum flow rate of the other gas stream. The present results demonstrate that each gas stream governs breakup through different mechanisms and that neither is universally dominant.

The analysis of the breakup modes observed under the operating conditions shown in Fig. 3 suggests that all share the same underlying mechanism: the formation of a bubble. Consequently, such regimes are henceforth referred to as **bubble-induced** breakup modes. If the bubble remains intact due to insufficient aerodynamic forces, the breakup corresponds to the classical **Rayleigh mode**. All other modes differ in terms of bubble shape and size prior to rupture, as well as the spatial arrangement of the resulting ligaments and large droplets after rupture, which is strongly influenced by the frequency of bubble bursting.

While the analysis of the influence of gas momentum flow rates is exemplarily based on the breakup mode classification shown in Fig. 3, the classifications in Figs. 4, 5 and A.1 provide equivalent plots for different liquid mass flow rates and liquid sheet thicknesses. These figures confirm the same dependencies on inner and outer gas flow rates, however, the variations in s_l and $\dot{M}_\mathrm{l}$ lead to the occurrence of additional breakup regimes. The additional regimes are **non-bubble-induced**, i.e., not characterized by bubble formation, and will be discussed in Section 3.2.

3.2. *Influence of liquid sheet thickness and liquid velocity*

As a second step, the influence of liquid sheet thickness and liquid velocity on the primary breakup dynamics is examined. The analysis is based on the breakup mode classifications presented in Figs. 4, 5 and A.1. As the sheet thickness s_l increases, the liquid velocity v_l decreases due to the constant mass flow rate. Conversely, for constant s_l, an increase in liquid mass flow rate $\dot{M}_\mathrm{l}$ leads to higher v_l.

In general, a thicker sheet implies a larger liquid mass, which requires stronger aerodynamic forces for deformation and acceleration. In **bubble-induced** breakup modes, this increased mass slows bubble growth because more liquid must be moved during expansion. Consequently, bubble rupture is delayed and the formation frequency decreases, as confirmed by high-speed imaging.

If bubble rupture is excessively delayed, aerodynamic forces may collapse the bubble before significant radial growth occurs. When these forces dominate, bubble formation can be completely suppressed. This marks the transition to **non-bubble-induced** breakup modes. Conversely, if aerodynamic forces are insufficient, the bubble continues to expand until the sheet becomes thin enough to rupture, shifting the breakup point along the flow direction and increasing radial extension compared to thinner sheets.

The liquid velocity v_l further influences this process by controlling the interaction time between gas and liquid in regions of high shear rates. Lower v_l (due to larger s_l at constant $\dot{M}_\mathrm{l}$) prolongs this interaction, enhancing aerodynamic effects and promoting sheet disintegration before bubbles can grow significantly or even form. In contrast, increasing $\dot{M}_\mathrm{l}$ from 30 to 60 and 90 kg h^{-1} at constant s_l raises v_l, reducing interaction time and favoring bubble formation and growth, as reflected by higher bubble formation frequencies. Thus, prolonged residence in regions of high shear rates tends to suppress bubble formation and drives transitions towards **non-bubble-induced** breakup modes.

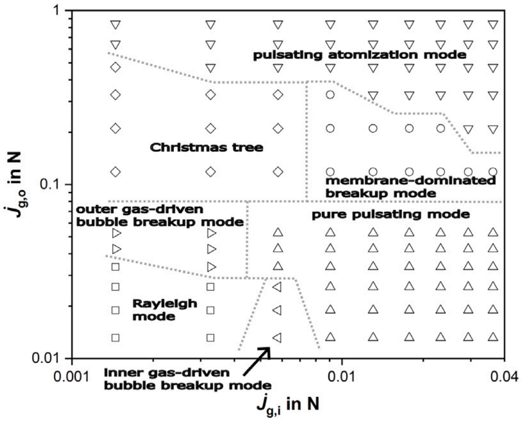

s_l **= 1 mm** (v_l = 1.3 m·s^{-1})

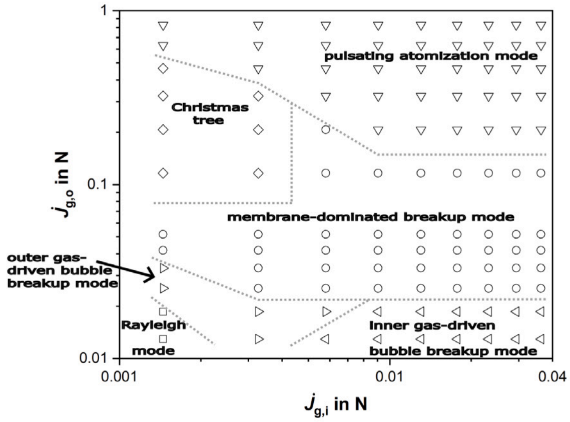

s_l **= 2 mm** (v_l = 0.5 m·s^{-1})

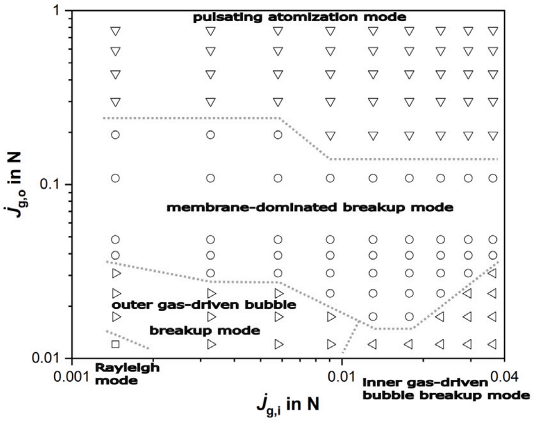

s_l **= 3 mm** (v_l = 0.3 m·s^{-1})

Fig. 4. Breakup mode classification from HSC images for $\dot{M}_\mathrm{l}$ = 60 kg h^{-1}, shown as function of inner and outer gas momentum flow rate ($\dot{J}_\mathrm{g,i}$ and $\dot{J}_\mathrm{g,o}$) for different liquid sheet thicknesses s_l = 1, 2 and 3 mm.

As shown in Fig. 4, increasing s_l causes the regions where breakup modes characterized by regular rupture and bubble formation – such as the **Christmas tree** and **pure pulsating mode** – occur to progressively shrink and eventually disappear at s_l = 3 mm. As a result, the domain of the **membrane-dominated breakup mode** expands significantly. This shift is primarily driven by the reduced liquid velocity associated with larger s_l, which prolongs the interaction between gas and liquid in regions of high shear rates. Extended interaction favors the formation of large membranes typical for this regime. A similar trend is observed for the **Rayleigh mode**, which also relies on regular bubble formation.

In contrast, the **pulsating atomization mode** shifts towards lower inner gas momentum flow rates as s_l increases. This shift reflects the influence of prolonged gas–liquid contact in regions of high shear rates.

Similar effects observed for $\dot{M}_l = 60$ kg h^{-1} in Fig. 4 are also evident in Fig. A.1, where a liquid mass flow rate of $\dot{M}_l = 90$ kg h^{-1} is investigated. Furthermore, comparable trends are found in the investigation at $\dot{M}_l = 30$ kg h^{-1} shown in Fig. 5. However, additional **non-bubble-induced** modes emerge, which – as previously explained – are promoted by increased liquid sheet thickness and reduced liquid velocity. Due to the lowest liquid velocities, such modes appear exclusively in the breakup mode classification in Fig. 5.

The **Rayleigh mode** is already limited at $s_l = 1$ mm and vanishes entirely as s_l increases, transitioning into the **beads-on-a-string mode** at $s_l = 3$ mm (Fig. 5). The **beads-on-a-string mode** (Fig. 2(viii)) is characterized by a chain-like pattern. A slender gas jet forms within the liquid sheet, similar to the jetting regime described by Sevilla et al. (2005) and Gañán-Calvo et al. (2006). As the gas jet ruptures due to the inward-impinging liquid, bead-like structures emerge. These beads break into individual droplets along the flow direction, whereas the connecting liquid column disintegrates into satellite droplets.

In the breakup mode classification shown in Fig. 5 the region where the **pure pulsating mode** occurs also diminishes, transitioning into the newly identified **membrane-like breakup mode** (Fig. 2(ix)). This mode resembles the membrane-type breakup reported by Chigier and Faragó (1992) for jet nozzles and the stretched streamwise ligament breakup described by Stapper and Samuelsen (1990) for sheet nozzles. It is characterized by the formation of thin liquid membranes at distinct positions on the liquid surface, which stretch in the flow direction, elongate, thin out and eventually rupture into fine droplets. Although the formation of a bubble can occur, it is rare. When present, these bubbles typically collapse immediately without significant radial expansion, making this a **non-bubble-induced** breakup mode. The region of the **membrane-like mode** significantly expands towards lower inner and higher outer gas momentum flow rates at $s_l = 3$ mm. As a result, regions where the **membrane-dominated breakup mode** occurs for smaller liquid sheet thicknesses transitions into the **membrane-like mode** for $s_l = 3$ mm due to the absence of bubble formation.

The region of the **pulsating atomization mode** shrinks with increasing s_l and is gradually replaced by the **prompt atomization mode** (Fig. 2(x)). In this regime, strong aerodynamic forces cause immediate sheet disintegration at the nozzle exit, without bubble formation. This mode is typically accompanied by oscillations around the axis and the absence of pulsating spray pattern.

At $s_l = 3$ mm, another regime becomes dominant: the **fiber type breakup mode** (Fig. 2(xi)). This mode shows strong resemblance to the *fiber breakup* reported by Chigier and Faragó (1992) for jet nozzles and is characterized by nearly complete suppression of bubble formation, likely due to the high momentum flow rate of the outer gas stream. Formed bubbles collapse immediately, preventing any significant radial growth. Instead, thin, thread-like ligaments detach from the rim of the liquid sheet and stretch axially before disintegrating into fine droplets. Unlike the **prompt atomization mode**, this regime features a longer primary breakup length.

At constant liquid mass flow rate, increasing s_l has two distinct effects on the breakup pattern, which become particularly evident in the regime classification shown in Fig. 5. When the sheet thickness is increased to 2 mm, the prolonged interaction of the liquid with the gas in regions of high shear rates shortens the primary breakup length, as indicated by the transition from the **pulsating** to the **prompt atomization mode**. A further increase to $s_l = 3$ mm reverses this trend: The breakup length becomes significantly longer because the available gas momentum flow rate is largely consumed before reaching the liquid core – even when gas is supplied from both sides of the sheet – as reflected by the transition to the **fiber type breakup mode**, see Fig. 2.

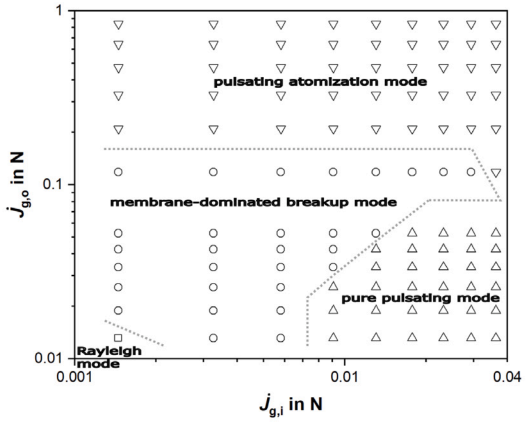

s_l = **1 mm** ($v_l = 0.6$ m·s^{-1})

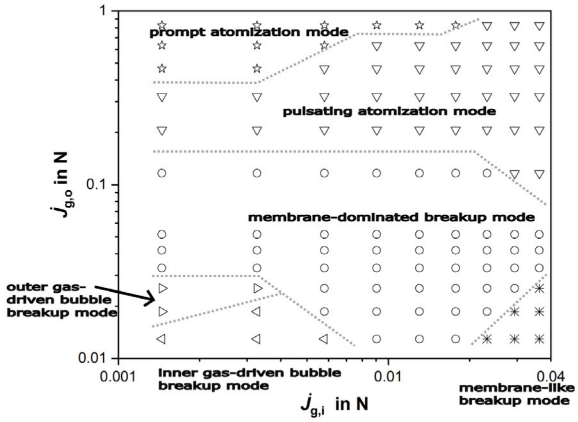

s_l = **2 mm** ($v_l = 0.3$ m·s^{-1})

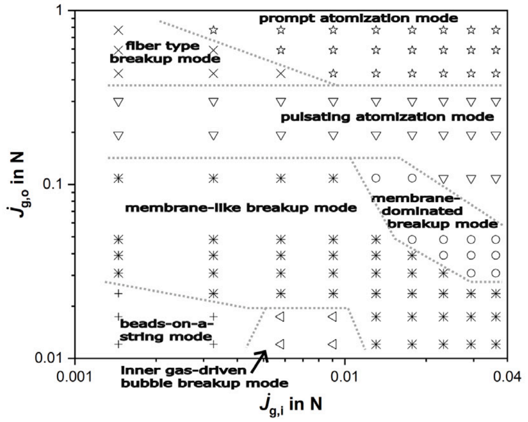

s_l = **3 mm** ($v_l = 0.1$ m·s^{-1})

Fig. 5. Breakup mode classification from HSC images for $\dot{M}_l = 30$ kg h^{-1}, shown as function of inner and outer gas momentum flow rate ($\dot{J}_{g,i}$ and $\dot{J}_{g,o}$) for different liquid sheet thicknesses $s_l = 1$, 2 and 3 mm.

At constant liquid sheet thickness, an increase in mass flow rate leads to higher liquid velocities and elevated bubble formation frequencies. Consequently, atomization modes characterized by frequent bubble formation – such as **Rayleigh**, **Christmas tree** and **pure pulsating mode** – expand their domains of occurrence. In contrast, the regions associated with **non-bubble-induced** modes diminish accordingly (Figs. 4, 5 and A.1).

3.3. Applying and predicting breakup modes for nozzle design

As a third step, the objective is to examine and predict breakup modes that are technically relevant. For this purpose, a ratio-based design approach was developed to support nozzle design for high liquid mass flow rates, thereby enabling predictive scaling by identifying the conditions for transition to technically relevant breakup modes.

3.3.1. Technically relevant breakup modes and operating ranges

The **fiber** and **prompt atomization mode** are well established for twin-fluid jet nozzles as primary breakup regimes that generate fine sprays. From a technical perspective, the relevance of a breakup mode is primarily determined by its capability to generate fine sprays. Therefore, these modes are considered technically significant. Examination of the HSC images in Fig. 2 indicates that, towards the lower edges of each frame, the spray produced in close proximity to the nozzle in the **fiber** and **prompt atomization mode** exhibit droplet sizes and overall spray quality comparable to those achieved by the **pulsating atomization mode**. For this reason, the **pulsating atomization mode** is included among the technically relevant regimes. The **prompt atomization mode** is particularly significant due to its ability to produce non-pulsating, fine sprays. However, as shown in Figs. 4, 5 and A.1, this mode occurs only within a very narrow operating range. In the investigated parameter space, this mode was exclusively observed for the largest sheet thicknesses ($s_{\mathrm{l}} = 2$ and 3 mm) and the lowest mass flow rate ($\dot{M}_{\mathrm{l}} = 30$ kg h^{-1}), corresponding to the lowest liquid velocities studied. For these conditions, the outer gas momentum flow rate must exceed approximately 0.4 N.

With increasing sheet thickness, the operating range of the **prompt atomization mode** shifts towards higher inner gas momentum flow rates, which is consistent with the requirement for strong aerodynamic forces on both sides of the liquid layer to achieve complete disintegration immediately beneath the nozzle exit. At lower inner gas momentum flow rates, the reduced shear forces result in longer breakup lengths, leading to the occurrence of the **fiber type breakup mode**, which also appears only within a limited operating range.

In contrast, the **pulsating atomization mode** is present across a wide range of operating conditions and appears in all breakup mode classifications and for all sheet thicknesses. A minimum outer gas momentum flow rate is always required to trigger this mode, typically ranging between $\dot{J}_{\mathrm{g,o}} = 0.1$ N and 0.6 N depending on sheet thickness and operating conditions. Once this threshold is exceeded, the **pulsating atomization mode** persists over a broad range of inner gas momentum flow rates.

3.3.2. Ratio-based design approach

To quantify the aerodynamic effort required per unit of liquid mass, the ratios $\dot{J}_{\mathrm{g,i}}/\dot{M}_{\mathrm{l}}$ and $\dot{J}_{\mathrm{g,o}}/\dot{M}_{\mathrm{l}}$ are introduced. A direct comparison of absolute gas momentum flow rates is insufficient because the aerodynamic force needed for sheet deformation and disintegration scales with the liquid mass flow rate (Figs. 4, 5 and A.1). These ratios provide:

- Direct comparison across different operating conditions (e.g., varying liquid mass flow rates).
- Identification of threshold values associated with specific breakup regimes.
- A basis for extrapolating the observed trends from laboratory to larger-scale systems.

Based on this approach, three diagrams are presented, with each diagram corresponding to one liquid mass flow rate. In Fig. 6, $\dot{J}_{\mathrm{g,o}}/\dot{M}_{\mathrm{l}}$ is shown as a function of $\dot{J}_{\mathrm{g,i}}/\dot{M}_{\mathrm{l}}$ and data from all investigated liquid sheet thicknesses are included. The open circles denote breakup modes that are not considered relevant for technical applications, whereas the closed circles represent those classified as relevant.

In all three diagrams, it becomes evident that with increasing liquid sheet thickness, the domains associated with technically relevant breakup modes shift towards lower values of $\dot{J}_{\mathrm{g,i}}/\dot{M}_{\mathrm{l}}$ and $\dot{J}_{\mathrm{g,o}}/\dot{M}_{\mathrm{l}}$. To illustrate the influence of the liquid mass flow rate on the transition between technically relevant and irrelevant breakup modes, a gray transition line is applied in all three diagrams, exemplarily for a liquid sheet thickness of 3 mm. This sheet thickness was selected because it represents the upper end of the investigated range and is particularly relevant for assessing scalability.

For all three mass flow rates, a consistent trend is observed: With increasing $\dot{J}_{\mathrm{g,i}}/\dot{M}_{\mathrm{l}}$, the required $\dot{J}_{\mathrm{g,o}}/\dot{M}_{\mathrm{l}}$ initially decreases until a distinct inflection point is reached. Beyond this point, $\dot{J}_{\mathrm{g,o}}/\dot{M}_{\mathrm{l}}$ remains approximately constant, regardless of further increases of $\dot{J}_{\mathrm{g,i}}/\dot{M}_{\mathrm{l}}$.

As the liquid mass flow rate increases, the inflection point shifts towards lower values of $\dot{J}_{\mathrm{g,i}}/\dot{M}_{\mathrm{l}}$. Moreover, the plateau region, where $\dot{J}_{\mathrm{g,o}}/\dot{M}_{\mathrm{l}}$ remains constant, does not vary with increasing $\dot{M}_{\mathrm{l}}$. For all three values of $\dot{M}_{\mathrm{l}}$, the transition curves intersect the vertical axis at an identical value of $\dot{J}_{\mathrm{g,o}}/\dot{M}_{\mathrm{l}} = 0.00503$ N/(kg h^{-1}), and the plateau level stabilizes at $\dot{J}_{\mathrm{g,o}}/\dot{M}_{\mathrm{l}} = 0.00214$ N/(kg h^{-1}).

For constant s_{l}, $\dot{M}_{\mathrm{l}}$ increases by increments in v_{l}, thereby shortening the interaction time between liquid and gas in regions of high shear rates. As previously discussed in Section 3.2, this reduced interaction promotes higher bubble formation frequency, which accelerates the transition between breakup modes. In general, analysis of $\dot{J}_{\mathrm{g,i}}/\dot{M}_{\mathrm{l}}$ and $\dot{J}_{\mathrm{g,o}}/\dot{M}_{\mathrm{l}}$ shows that with increasing $\dot{M}_{\mathrm{l}}$, the absolute values of $\dot{J}_{\mathrm{g,i}}$ and $\dot{J}_{\mathrm{g,o}}$ required to reach technically relevant breakup modes also increase, although the rate of increase diminishes. This indicates a nonlinear relationship between $\dot{M}_{\mathrm{l}}$ (and thus v_{l}) and the required gas momentum flow rates, which becomes evident through the ratio-based representation and is illustrated by the gray transition lines.

The gray transition lines provide an empirical basis for quantifying the observed trends and nozzle design. To capture the dependence on $\dot{M}_{\mathrm{l}}$, a potential fit according to Eq. (5) is applied. The fit parameters are determined via the least-square method, yielding a coefficient of determination of $R^2 = 0.99$, which indicates good agreement with the experimental data and supports the applicability of the approach to describe the transition between technically relevant and non-relevant breakup modes:

$$\frac{\dot{J}_{\mathrm{g,o}}}{\dot{M}_{\mathrm{l}}} = -\left(0.0006\ (\mathrm{h/kg})^{2.4522} \cdot \dot{M}_{\mathrm{l}}^{2.4522}\right) \cdot \frac{\dot{J}_{\mathrm{g,i}}}{\dot{M}_{\mathrm{l}}} + 0.00503\ \mathrm{N/(kg\ h^{-1})} \tag{5}$$

The liquid mass flow rate must be entered in Eq. (5) in the unit kg h^{-1} and the ratio $\dot{J}_{\mathrm{g,i}}/\dot{M}_{\mathrm{l}}$ in N/(kg h^{-1}). Eq. (5) describes the linearly decreasing parts on the transition lines. For any given value of $\dot{J}_{\mathrm{g,i}}/\dot{M}_{\mathrm{l}}$, the corresponding $\dot{J}_{\mathrm{g,o}}/\dot{M}_{\mathrm{l}}$ can be computed using Eq. (5). If the calculated value is greater than or equal to the plateau level of $\dot{J}_{\mathrm{g,o}}/\dot{M}_{\mathrm{l}} = 0.00214$ N/(kg h^{-1}), the operating point lies on the linearly decreasing branch, and the value obtained from Eq. (5) is valid. If the computed value falls below this threshold, the operating point lies within the plateau region, where $\dot{J}_{\mathrm{g,o}}/\dot{M}_{\mathrm{l}} = 0.00214$ N/(kg h^{-1}) applies independently of $\dot{J}_{\mathrm{g,i}}/\dot{M}_{\mathrm{l}}$. Eq. (5) therefore indicates whether a given $\dot{J}_{\mathrm{g,i}}/\dot{M}_{\mathrm{l}}$ lies in the descending portion of the transition line or in the plateau region. This approach provides a robust framework for estimating gas momentum requirements across varying liquid mass flow rates and is derived in accordance to the velocity range presented in Table 3.

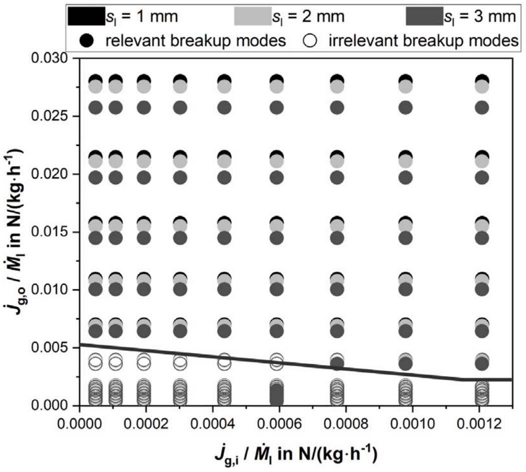

$\dot{M}_l$ = 30 kg·h^{-1}

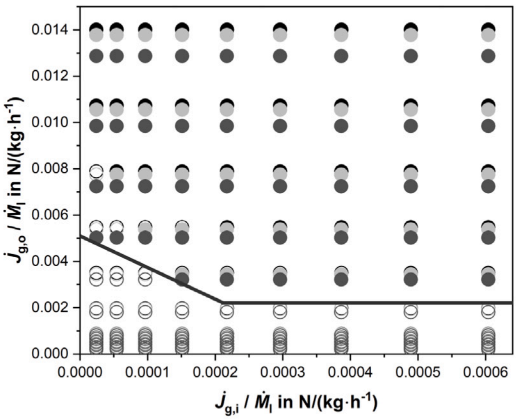

$\dot{M}_l$ = 60 kg·h^{-1}

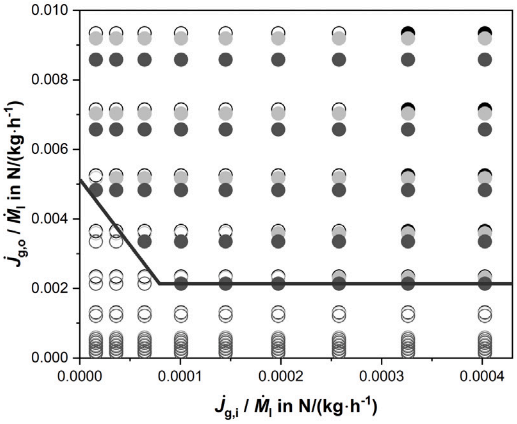

$\dot{M}_l$ = 90 kg·h^{-1}

Fig. 6. Operating ranges of breakup modes relevant for industrial applications for sheet thicknesses s_l = 1, 2 and 3 mm, shown as a function of inner and outer gas momentum flow rate divided by liquid mass flow rate ($\dot{J}_{g,i}/\dot{M}_l$ and $\dot{J}_{g,o}/\dot{M}_l$), for different liquid mass flow rates $\dot{M}_l$ = 30, 60 and 90 kg h^{-1}.

4. Summary and conclusion

In the present study, three dual gas-assisted annular sheet nozzles with three sheet thicknesses (1, 2 and 3 mm) were investigated. Annular sheet nozzle geometry was adapted to provide identical inner and identical outer gas orifice areas, allowing for constant gas momentum flow rates at fixed gas velocities while varying the liquid sheet thickness. The influence of inner and outer gas stream, liquid stream and liquid sheet thickness on primary sheet breakup was investigated over a broad range of operating conditions. High-speed imaging was applied to analyze the primary breakup process.

Key findings include:

1. A total of eleven distinct breakup modes were identified and classified into two main categories: (i) bubble-induced and (ii) non-bubble-induced modes, distinguished by the presence or absence of bubble formation.
2. Breakup classification maps were proposed, applying outer vs. inner gas momentum flow rate for different liquid velocities and each liquid sheet thickness.
3. The fiber type, prompt atomization, and pulsating atomization mode appear to be the most promising in producing fine sprays.
4. An empirical nozzle design approach was derived to describe the transition between technically relevant and non-relevant breakup modes. The approach is based on ratios of inner and outer gas momentum flow rates to the liquid mass flow rate, which quantify the aerodynamic effort per unit of liquid mass. This approach enables a comparison under different operating conditions and provides a basis for nozzle design targeting specific breakup regimes at elevated liquid mass flow rates.

CRediT authorship contribution statement

Juliana Richter: Writing – original draft, Visualization, Validation, Investigation, Formal analysis, Conceptualization. **Tobias Jakobs:** Writing – review & editing, Supervision, Conceptualization. **Frederik Scheiff:** Supervision. **Thomas Kolb:** Writing – review & editing, Supervision, Conceptualization.

Declaration of Generative AI and AI-assisted technologies in the writing process

During the preparation of this work the authors used Copilot in order to improve the language of the manuscript. After using this tool, the authors reviewed and edited the content as needed and take full responsibility for the content of the published article.

Declaration of competing interest

The authors declare that they have no known competing financial interests or personal relationships that could have appeared to influence the work reported in this paper.

Acknowledgments

The authors gratefully acknowledge the financial support by the Helmholtz Association of German Research Centres, within the research field Energy, program Materials and Technologies for the Energy Transition (MTET) (38.05.01).

Appendix A. Regime classifications

See Fig. A.1.

Appendix B. Supplementary data

Supplementary material related to this article can be found online at https://doi.org/10.1016/j.ijmultiphaseflow.2026.105736.

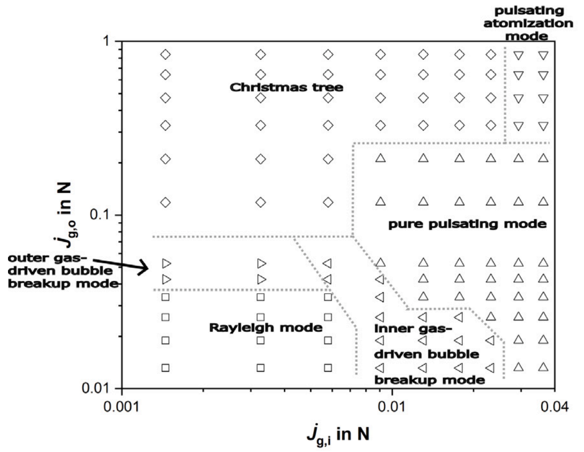

s_l = 1 mm (v_l = 1.9 m·s^{-1})

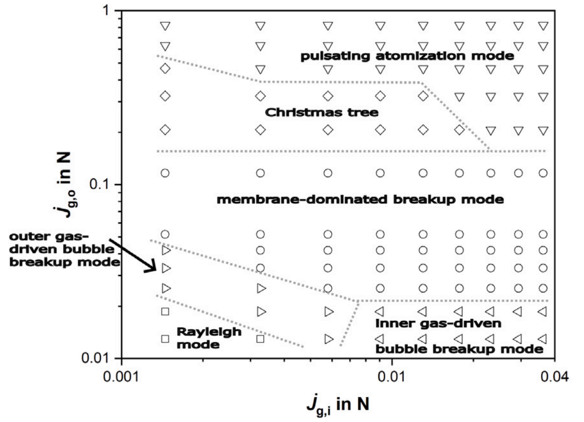

s_l = 2 mm (v_l = 0.8 m·s^{-1})

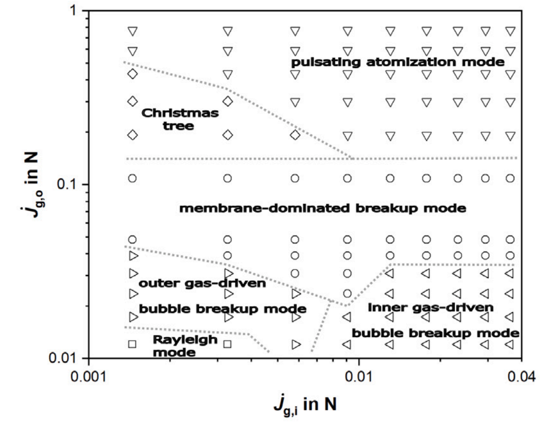

s_l = 3 mm (v_l = 0.4 m·s^{-1})

Fig. A.1. Breakup mode classification from HSC images for $\dot{M}_l$ = 90 kg h^{-1}, shown as function of inner and outer gas momentum flow rate ($\dot{J}_{g,i}$ and $\dot{J}_{g,o}$) for different liquid sheet thicknesses s_l = 1, 2 and 3 mm.

Data availability

Data will be made available on request.

References

Adzic, M., Carvalho, I.S., Heitor, M.V., 2001. Visualization of the disintegration of an annular liquid sheet in a coaxial airblast injector at low atomizing air velocities. Optics 5 (1), 27–38.

Alajmi, A.E.S.E.T., Adam, N.M., Hairuddin, A.A., Abdullah, L.C., 2019. Fuel atomization in gas turbines: A review of novel technology. Int. J. Energy Res. 43 (8), 3166–3181. http://dx.doi.org/10.1002/er.4415.

Bohl, W., Elmendorf, W., 2014. Technische Strömungslehre, 15 Vogel, Würzburg.

Carisson, P., Gebart, R., Grönberg, C., Marklund, M., Risberg, M., Wiinikka, H., Öhrman, O., 2009. Spatially resolved measurements of gas composition in a pressurised black liquor gasifier. Environ. Prog. Sustain. Energy 28 (3), 316–323. http://dx.doi.org/10.1002/ep.10380.

Carvalho, I.S., Heitor, M.V., 1998. Liquid film break-up in a model of a prefilming airblast nozzle. Exp. Fluids 24 (24), 408–415. http://dx.doi.org/10.1007/s003480050190.

Cejpek, O., Maly, M., Avulapati, M.M., Jedelsky, J., 2025. Suitability of different twin-fluid atomizer types for CO$_2$ capture in spray columns. ICLASS (International Conf. Liq. At. Spray Systems) http://dx.doi.org/10.2218/iclass.2021.6016.

Chatterjee, S., Das, M., Mukhopadhyay, A., Sen, S., 2015. Experimental investigation of breakup of annular liquid sheet in a hybrid atomizer. J. Propuls. Power 31 (5), 1232–1241. http://dx.doi.org/10.2514/1.B35574.

Chigier, N., Faragó, Z., 1992. Morphological classification of disintegration of round liquid jets in a coaxial air stream. At. Sprays 2 (2), 137–153. http://dx.doi.org/10.1615/AtomizSpr.v2.i2.50.

Choi, C.J., Lee, S.Y., 1997. Disintegration of annular liquid sheets with core air flow - mode classification. ICLASS (International Conf. Liq. At. Spray Systems) 24 (1–3), http://dx.doi.org/10.1615/InterJFluidMechRes.v24.i1-3.400.

Fu, H., Li, X., Prociw, L., Hu, T., 2003. Experimental investigation on the breakup of annular liquid sheets in two co-flowing airstreams. In: 1st International Energy and Conversion Engineering Conference.. http://dx.doi.org/10.2514/6.2003-5944.

Gañán-Calvo, A.M., Herrada, M.A., Garstecki, P., 2006. Bubbling in unbounded coflowing liquids. Phys. Rev. Lett. 96 (12), 124504. http://dx.doi.org/10.1103/PhysRevLett.96.124504.

Haas, M., Dammann, M., Fleck, S., Kolb, T., 2023. Entrained flow gasification: Impact of fuel spray distribution on reaction zone structure. Fuel 334 (4), 126572. http://dx.doi.org/10.1016/j.fuel.2022.126572.

Haas, M., Fleck, S., Jakobs, T., Kolb, T., 2025. Liquid fuel evaporation under entrained flow gasification conditions – insights for burner development. Therm. Sci. Eng. Prog. 59, 103342. http://dx.doi.org/10.1016/j.tsep.2025.103342.

Haidn, O.J., Habiballah, M., 2003. Research on high pressure cryogenic combustion. Aerosp. Sci. Technol. 7 (6), 473–491. http://dx.doi.org/10.1016/S1270-9638(03)00052-X.

Ibrahim, A.A., Jog, M.A., 2008. Nonlinear instability of an annular liquid sheet exposed to gas flow. Int. J. Multiph. Flow 34 (7), 647–664. http://dx.doi.org/10.1016/j.ijmultiphaseflow.2007.12.003.

Karlsruhe Institute of Technology, Virtual Spray Test Rig (VSTR). https://www.itc.kit.edu/390.php, https://vbt.ebi.kit.edu/english/1135.php. (Accessed 03 December 2025).

Kendall, J.M., 1986. Experiments on annular liquid jet instability and on the formation of liquid shells. Phys. Fluids 29 (7), 2086. http://dx.doi.org/10.1063/1.865595.

Kuznetsov, G., Podgornaya, E., Strizhak, P., Volkov, R., 2024. Impact of atomizer design on slurry fuel atomization behavior. Phys. Fluids 36, 107166. http://dx.doi.org/10.1063/5.0220879.

Lasheras, J.C., Hopfinger, E.J., 2000. Liquid jet instability and atomization in a coaxial gas stream. Annu. Rev. Fluid Mech. 32 (1), 275–308. http://dx.doi.org/10.1146/annurev.fluid.32.1.275.

Lavergne, G., Trichet, P., Hebrard, P., Biscos, Y., 1993. Liquid sheet disintegration and atomization on a simplified airblast atomizer. J. Eng. Gas Turbines Power (115), 461–466. http://dx.doi.org/10.1115/92-GT-107.

Leboucher, N., Roger, F., Carreau, J.-L., 2010. Disintegration process of an annular liquid sheet assisted by coaxial gaseous coflow(s). At. Sprays (20), 847–862. http://dx.doi.org/10.1615/AtomizSpr.v20.i10.20.

Lefebvre, A., 1992. Twin-fluid atomization factors influencing mean drop size. At. Sprays 2, 101–119. http://dx.doi.org/10.1615/AtomizSpr.v2.i2.30.

Leroux, B., Delabroy, O., Lacas, F., 2007. Experimental study of coaxial atomizers scaling. Part 1: Dense core zone. At. Sprays 17, 381–407. http://dx.doi.org/10.1615/AtomizSpr.v17.i5.10.

Martínez, B., Ángel, M., Prithika, R., Alarcón, S., Nicolás, J., Volker, G., 2025. Atomizing high-viscosity non-Newtonian fluids with the ACLR nozzle: Correlation between internal flow and external spray instabilities. J. Non-Newton. Fluid Mech. 338, 105405. http://dx.doi.org/10.1016/j.jnnfm.2025.105405.

Mlkvik, M., Stähle, P., Schuchmann, H.P., Gaukel, V., Jedelsky, J., Jicha, M., 2015. Twin-fluid atomization of viscous liquids: The effect of atomizer construction on breakup process, spray stability and droplet size. Int. J. Multiph. Flow 77, 19–31. http://dx.doi.org/10.1016/j.ijmultiphaseflow.2015.06.010.

Muthukrishnan, S., Tan, X., Srinivasan, V., 2023. High-efficiency spray cooling of rough surfaces with gas-assist atomization. Appl. Therm. Eng. 221, 119764. http://dx.doi.org/10.1016/j.applthermaleng.2022.119764.

Peteinaris, A., Terzis, A., 2025. Water-sheet atomization and spray characterization from convergent nozzles. Phys. Fluids 37 (12), http://dx.doi.org/10.1063/5.0307029.

Rajmohan, B., Reddy, S.N., Meikap, B.C., 2008. Removal of SO_2 from industrial effluents by a novel twin-fluid air-assist atomized spray scrubber. Ind. Eng. Chem. Res. 47, 7833–7840. http://dx.doi.org/10.1021/ie800712a.

Risberg, M., Marklund, M., 2009. Visualizations of gas-assisted atomization of black liquor and syrup/water mixtures at elevated ambient pressures. At. Sprays 19, 957–967. http://dx.doi.org/10.1615/AtomizSpr.v19.i10.40.

Sänger, A., 2018. Zerstäubung hochviskoser Fluide bei variierendem Systemdruck - Grundlagenforschung zur Hochdruck-Flugstromvergasung Dissertation. Karlsruher Institut für Technologie (KIT), Karlsruhe, http://dx.doi.org/10.5445/IR/1000087397.

Sänger, A., Jakobs, T., Djordjevic, N., Kolb, T., 2014. Effect of primary instability of a high viscous liquid jet on the spray quality generated by a twin-fluid atomizer. In: ILASS – Europe 2014, 26th Annual Conference on Liquid Atomization and Spray Systems. http://dx.doi.org/10.5445/IR/1000129940.

Sevilla, A., Gordillo, J.M., Martínez-Bazán, C., 2005. Transition from bubbling to jetting in a coaxial air–water jet. At. Sprays 17 (1), 018105. http://dx.doi.org/10.1063/1.1831312.

Shen, J., Li, X., 1996. Breakup of annular viscous liquid jets in two gas streams. J. Propuls. Power 12 (4), 752–759. http://dx.doi.org/10.2514/3.24098.

Sikka, R., Vågsæther, K., Bjerketvedt, D., Lundberg, J., 2021. Experimental study of primary atomization characteristics of sonic air-assist atomizers. Appl. Sci. 11 (21), 10444. http://dx.doi.org/10.3390/app112110444.

Sivakumar, D., Kulkarni, V., 2011. Regimes of spray formation in gas-centered swirl coaxial atomizers. Exp. Fluids 51 (3), 587–596. http://dx.doi.org/10.1007/s00348-011-1073-7.

Stapper, B.E., Samuelsen, G.S., 1990. An experimental study of the breakup of a two-dimensional liquid sheet in the presence of co-flow air shear. In: AIAA – 28th Aerospace Sciences Meeting. http://dx.doi.org/10.2514/6.1990-461.

Tian, X.-S., Zhao, H., Liu, H.-F., Li, W.-F., Xu, J.-L., 2014. Effect of central tube thickness on wave frequency of coaxial liquid jet. Fuel Process. Technol. 119, 190–197. http://dx.doi.org/10.1016/j.fuproc.2013.11.011.

Varga, C.M., Lasheras, J.C., Hopfinger, E.J., 2003. Initial breakup of a small-diameter liquid jet by a high-speed gas stream. J. Fluid Mech. (497), 405–434. http://dx.doi.org/10.1017/S0022112003006724.

Wachter, S., Jakobs, T., Kolb, T., 2021a. Comparison of central jet and annular sheet atomizers at identical gas momentum flows. Ind. Eng. Chem. Res. 60 (30), 11502–11512. http://dx.doi.org/10.1021/acs.iecr.1c01526.

Wachter, S., Jakobs, T., Kolb, T., 2021b. Effect of gas jet angle on primary breakup and droplet size applying coaxial gas-assisted atomizers. ICLASS (International Conf. Liq. At. Spray Systems) 1 (1), http://dx.doi.org/10.2218/iclass.2021.5808.

Wachter, S., Jakobs, T., Kolb, T., 2022. Mass flow scaling of gas-assisted coaxial atomizers. Appl. Sci. 12 (4), 2123. http://dx.doi.org/10.3390/app12042123.

Wahono, S., Honnery, D., Soria, J., Ghojel, J., 2008. High-speed visualisation of primary break-up of an annular liquid sheet. Exp. Fluids 44 (3), 451–459. http://dx.doi.org/10.1007/s00348-007-0361-8.

Wang, G., Zhang, T., Song, C., Yu, X., Shan, C., Gu, H., Lan, Y., 2023. Evaluation of spray drift of plant protection drone nozzles based on wind tunnel test. Agriculture 13 (3), 628. http://dx.doi.org/10.3390/agriculture13030628.

Ye, K., Hu, G., Tong, Z., Xu, Y., Zheng, J., 2025. Key intelligent pesticide prescription spraying technologies for the control of pests, diseases, and weeds: A review. Agriculture 15 (1), 81. http://dx.doi.org/10.3390/agriculture15010081.

Yuan, F., Gu, C., Yi, K., Dou, H., Li, S., Yang, S., Zou, W., Zhai, C., 2023. Atomization characteristics of a hollow cone nozzle for air-assisted variable-rate spraying. Agriculture 13 (10), http://dx.doi.org/10.3390/agriculture13101992.

Zhang, F., Wachter, S., Zirwes, T., Jakobs, T., Zarzalis, N., Trimis, D., Kolb, T., Stapf, D., 2023. Effect of nozzle upscaling on coaxial, gas-assisted atomization. Phys. Fluids 35 (4), http://dx.doi.org/10.1063/5.0141156.

Zhao, H., Hou, Y.-B., Liu, H.-F., Tian, X.-S., Xu, J.-L., Li, W.-F., Liu, Y., Wu, F.-Y., Zhang, J., Lin, K.-F., 2014a. Influence of rheological properties on air-blast atomization of coal water slurry. J. Non-Newton. Fluid Mech. 211, 1–15. http://dx.doi.org/10.1016/j.jnnfm.2014.06.007.

Zhao, H., Liu, H.-F., Tian, X.-S., Xu, J.-L., Li, W.-F., Lin, K.-F., 2014b. Influence of atomizer exit area ratio on the breakup morphology of coaxial air and round water jets. AIChE J. 60 (6), 2335–2345. http://dx.doi.org/10.1002/aic.14414.

Zhao, H., Liu, H.-F., Tian, X.-S., Xu, J.-L., Li, W.-F., Lin, K.-F., 2014c. Outer ligament-mediated spray formation of annular liquid sheet by an inner round air stream. Exp. Fluids 55 (8), 27. http://dx.doi.org/10.1007/s00348-014-1793-6.

Zhao, H., Xu, J.-L., Wu, J.-H., Li, W.-F., Liu, H.-F., 2015. Breakup morphology of annular liquid sheet with an inner round air stream. Chem. Eng. Sci. 137, 412–422. http://dx.doi.org/10.1016/j.ces.2015.06.062.

Zhao, Y., Yang, Q., Wu, F., Gong, S., Wei, H., Peng, Y., Sato, T., Ge, M., 2025. Experimental study of heat transfer and surface fluid morphology in gas-atomized spray cooling with long distance. Int. J. Therm. Sci. 221, 110482. http://dx.doi.org/10.1016/j.ijthermalsci.2025.110482.

Zhou, H., Ou, M., Dong, X., Zhou, W., Dai, S., Jia, W., 2024. Spraying performance and deposition characteristics of an improved air-assisted nozzle with induction charging. Front. Plant Sci. 15, 1309088. http://dx.doi.org/10.3389/fpls.2024.1309088.